The Astrophysical Journal, 1003:132 (14pp), 2026 June 1 https://doi.org/10.3847/1538-4357/ae6104

Carbonaceous Chondrites Provide Evidence for Late-stage Planetesimal Formation in a Pressure Bump

Nerea Gurrutxaga, Joanna Drążkowska, Vignesh Vaikundaraman, and Thorsten Kleine
Max Planck Institute for Solar System Research, Justus-von-Liebig-Weg 3, Göttingen, 37077, Germany; gurrutxaga@mps.mpg.de
Received 2026 March 11; revised 2026 April 14; accepted 2026 April 16; published 2026 May 22

Abstract

Carbonaceous chondrites are samples from planetesimals that formed 2–4 million years after solar system formation began. They consist of distinct dust components formed at different times and locations in the accretion disk, and whose abundances in carbonaceous chondrites vary over planetesimal formation time. The mechanism that led to this time-varied accretion is not understood, but it is critical for understanding late-stage planetesimal formation. Using a two-dimensional Monte Carlo simulation of dust evolution, we show that differences in dust filtering and delivery rates of distinct dust components to a planet-induced pressure bump in the disk reproduce the observed compositions and formation ages of the carbonaceous chondrites. This implies that carbonaceous chondrites likely formed in a single, long-lived dust trap, most likely outside of Jupiter's orbit. Because differentiated meteorites, which sample an earlier generation of planetesimals, exhibit similar isotopic variability as the chondrites, they likely have also formed in dust traps, implying these structures were the dominant site for planetesimal formation in the solar system.

Unified Astronomy Thesaurus concepts: Meteorite composition (1037); Carbonaceous chondrites (200); Small Solar System bodies (1469); Protoplanetary disks (1300); Planet formation (1241); Monte Carlo methods (2238)

1. Introduction

The initial stages of planet formation span an enormous range of masses and involve the growth of tiny dust grains into kilometer-sized precursor objects called planetesimals (e.g., A. Johansen et al. 2014). As fragments of leftover planetesimals, meteorites provide a unique record of the conditions and timescales of the initial stages of planet formation in the solar system. Their ages and compositions reveal that planetesimal formation occurred at distinct locations and throughout almost the entire lifetime of the solar accretion disk (e.g., T. Kleine et al. 2020). Chondrite meteorites derive from parent bodies that formed late, between 2 and 4 million years (Myr) after solar system formation began (e.g., N. Sugiura & W. Fujiya 2014; K. Fukuda et al. 2022), and did not undergo significant melting and chemical differentiation. As such, they preserve a direct record of the distinct dust components that were combined to form their parent planetesimals. Chondrites, therefore, allow studying the processes by which small dust grains have been accreted into the first sizable planetary objects.

Among the chondrites, carbonaceous chondrites are the most primitive and diverse objects. They consist of refractory inclusions and chondrules embedded into a fine-grained matrix (E. R. D. Scott & A. N. Krot 2014). Refractory inclusions such as Ca-Al-rich inclusions (CAIs) are the oldest dated solids of the solar system and, as high-temperature condensates, they are thought to have formed near the young Sun before being transported outward by disk spreading or outflows (J. N. Cuzzi et al. 2003; F. J. Ciesla 2007). Chondrules are submillimeter-sized igneous spherules that formed by transient heating events of dust aggregates 2–4 Myr after CAI formation (e.g., A. N. Krot et al. 2009). The matrix contains relatively unprocessed submicron-sized mineral grains and is compositionally similar to the chemically most primitive chondrites, the Ivuna-type (CI) carbonaceous chondrites. Variations in the relative abundance of these three constituent components define the different groups of carbonaceous chondrites, each representing planetesimals that formed at different times and have distinct compositions (e.g., C. M. O. Alexander 2019; J. L. Hellmann et al. 2020). Moreover, refractory inclusion and chondrule abundances are correlated within each chondrite group, and matrix-poor chondrites appear to have formed earlier than matrix-rich chondrites (J. L. Hellmann et al. 2023). Only the Renazzo-type (CR) chondrites deviate from this trend because they are rich in chondrules but poor in refractory inclusions and matrix despite their relatively late formation time (D. L. Schrader et al. 2017; G. Budde et al. 2018).

Theoretical models indicate that planetesimal formation requires high concentrations of solid particles relative to gas (A. N. Youdin & J. Goodman 2005; J. Lim et al. 2024). This condition is difficult to achieve in disks with ages of 2–4 Myr, when the carbonaceous chondrites formed, because dust is efficiently depleted on a characteristic timescale of less than 1 Myr (J. Drążkowska et al. 2023). A common solution to this problem is to invoke dust enrichment and planetesimal formation in pressure bumps that, especially during the later stages of disk evolution, form in response to the presence of giant planets (P. Pinilla et al. 2012; S. M. Stammler et al. 2019; L. E. J. Eriksson et al. 2020). Indeed, it has been suggested that carbonaceous chondrites formed in a pressure bump outside Jupiter's orbit (S. J. Desch et al. 2018), and that their formation in a single pressure bump could potentially explain the trapping of refractory inclusions and chondrules (or their precursors) over a prolonged time (J. L. Hellmann et al. 2023). However, whether the temporal variations in the abundances

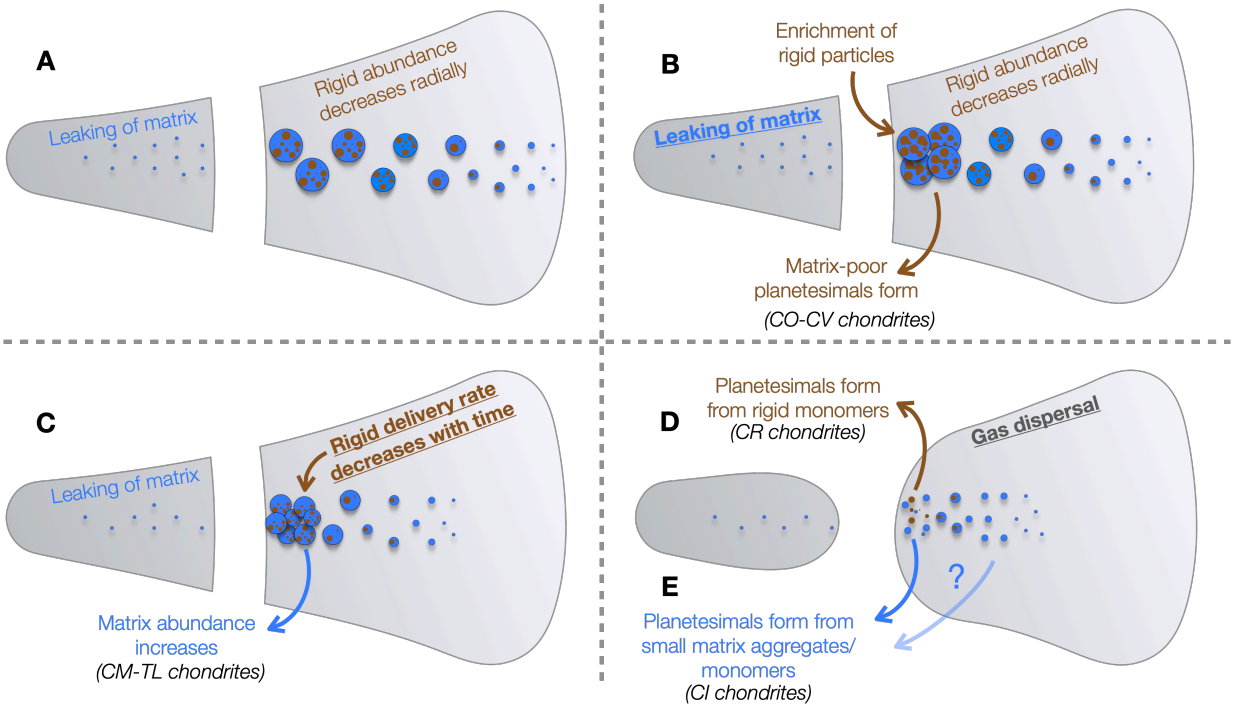

Figure 1. Schematic of the model for carbonaceous chondrite formation. We assume that chondrules and refractory inclusions are rigid particles, and that the matrix is fragile. Rigid and fragile materials can stick together to form larger pebbles. We highlight the dominant process at different times in bold and underlined. (A) Initially, ∼2 Myr after CAI formation, a gap is opened by a Jupiter-like planet. (B) Mostly fragile material passes through the gap, enriching the pressure bump with rigid particles. Planetesimal formation begins once the pebble-to-gas ratio becomes sufficiently high. (C) Then, the delivery of rigid particles to the pressure bump declines over time due to the faster radial drift (and thereby faster depletion in the outer disk) of the largest rigid monomers. (D) Afterward, photoevaporation reduces the gas surface density by orders of magnitude, and submillimeter-sized rigid particles reach pebble Stokes numbers. (E) Finally, as the gas density continues to decrease, particle sizes are further reduced to micrometer sizes. At this late stage, planetesimal formation may extend across the disk as the gap expands during photoevaporation.

of refractory inclusions and chondrules over matrix across the carbonaceous chondrite groups can be produced in a pressure bump has not yet been quantitatively explored. Addressing this question is of considerable interest, as it would allow determining the mechanism by which distinct dust components have been accreted into planetesimals, and how this mechanism may have changed over time.

Here, we present a model that combines gas disk evolution, planetesimal formation, and dust evolution, taking into account collisions between the different dust components present in carbonaceous chondrites. Figure 1 summarizes our model. In Section 2, we describe the gas disk model, the dust coagulation and fragmentation model for multiple dust components, and the setup of the simulations. In Section 3, we present the results of our simulations. In Section 4, we compare our results to the observed properties of carbonaceous chondrites, and we discuss the implications for understanding the origin of other chondrite parent bodies, as well as the origin of other meteorite parent bodies that formed earlier than the chondrites. We summarize our findings in Section 5.

2. Methods

2.1. Disk Model

We build a one-dimensional gas disk model that includes both disk formation and a planetary gap (Figure 2). We solve the viscous disk equations incorporating a source function that describes disk formation from the collapse of a rotating molecular cloud core using the publicly

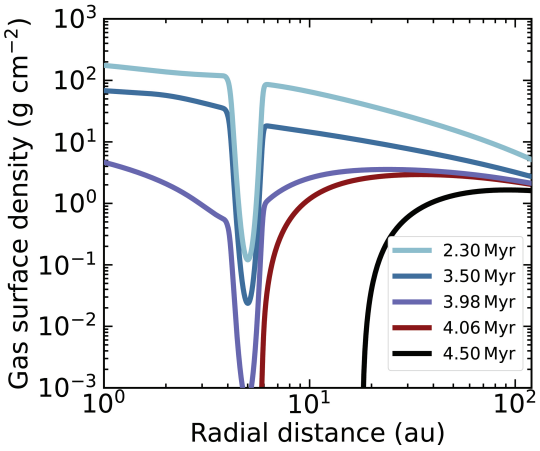

Figure 2. Gas surface density across the disk at different stages. A Jupiter-like planet opens a gap at 5 au. Disk dispersal by internal photoevaporation is included. Times are given relative to CAI formation, and the time difference between disk formation and CAI formation in our model is around 0.19 Myr.

available code `DD-Diskevol`[1](R. Hueso & T. Guillot 2005; J. Drążkowska & C. P. Dullemond 2018). Furthermore, we consider gas removal in the late evolutionary stages driven by internal photoevaporation, using a mass-loss rate derived by G. Picogna et al. (2021). The evolution of the gas surface

[1] https://github.com/astrojoanna/DD-diskevol

density is given by:

$$\frac{\partial \Sigma_g}{\partial t} = \frac{3}{r}\frac{\partial}{\partial r}\left[r^{1/2}\frac{\partial}{\partial r}(\nu \Sigma_g r^{1/2})\right] + \dot{\Sigma}_{g,inf} - \dot{\Sigma}_{g,PE}, \quad (1)$$

where r is the radial distance from the central star, Σ_g is the gas surface density, ν is the viscosity, $\dot{\Sigma}_{g,inf}$ is the infall rate (Equation (6) in R. Hueso & T. Guillot 2005), and $\dot{\Sigma}_{g,PE}$ is the mass-loss rate due to internal photoevaporation (Equations (6) and (7) in G. Picogna et al. 2021). We introduce the mass-loss rate term at 1 Myr after the onset of disk formation to avoid interfering with the early disk buildup phase, which starts with a gas surface density set to a floor value. As the disk evolves, the star mass increases in our model (see Figure 1 in J. Drążkowska & C. P. Dullemond 2018). However, the photoevaporation prescription of G. Picogna et al. (2021) is given for a fixed star mass. Since photoevaporation becomes significant at late evolutionary stages, when the star has already acquired most of its final mass, we adopt the photoevaporation model for a solar-mass star (see Table 2 in G. Picogna et al. 2021).

We assume that the disk is heated by viscous dissipation and stellar irradiation, and we adopt the opacities from K. R. Bell & D. N. C. Lin (1994; for further details, see R. Hueso & T. Guillot 2005, their Section 3.4.2). For the vertical structure, we assume a Gaussian gas density profile and isothermal temperature. To describe the viscosity ν, we employ the α-disk model (N. I. Shakura & R. A. Sunyaev 1973) given by:

$$\nu = \alpha_{acc} c_s H, \quad (2)$$

where α_{acc} is the dimensionless accretion rate, c_s is the sound speed, and H is the vertical scale height. $\alpha_{acc} \sim 10^{-2}$–$10^{-3}$ explains best the observed gas accretion rates toward young Sun-like stars and disk lifetimes of a few Myr (L. Hartmann et al. 1998). We choose $\alpha_{acc} = 5 \times 10^{-3}$, since this value corresponds to a disk lifetime of 4–5 Myr after CAI formation, consistent with estimates of the solar accretion disk lifetime derived from meteorite paleomagnetic studies (B. P. Weiss et al. 2021). Observations from dust settling, however, suggest that turbulence in the midplane must be lower ($\alpha_t \lesssim 10^{-4}$; C. Pinte et al. 2023). Therefore, we distinguish between the turbulence parameter $\alpha_t = 10^{-4}$ and the global accretion parameter $\alpha_{acc} = 5 \times 10^{-3}$.

To estimate the time difference between the onset of infall and the formation time of CAIs, we assume that CAIs condense at temperatures between 1400 and 1800 K. We then calculate the time at which the disk reaches this temperature range at the centrifugal radius (R. Hueso & T. Guillot 2005, their Equation (5)), as material can be transported outward beyond this location (S. Jongejan et al. 2023). For our chosen parameters, the time difference between the onset of infall and the formation of the first CAIs is 0.19 Myr.

Globally, the gas disk rotates at sub-Keplerian velocities, since the radially decreasing pressure gradient exerts an outward force that partially counteracts the gravitational force of the central star. The deviation from the Keplerian rotation is calculated by:

$$\Delta v = -\frac{1}{2}\frac{H}{r}\frac{\partial \ln P}{\partial \ln r} c_s, \quad (3)$$

where P is the gas pressure. Due to the relative velocity Δv between the orbital motion of the gas and that of solid particles, the gas exerts a drag force on the solids. Small dust particles respond rapidly to this drag force and remain well coupled to the gas motion. In contrast, larger solid particles, referred to as pebbles, do not respond quickly enough to the drag force and therefore undergo inward radial drift. Pressure bumps or substructures in the gas disk, such as planetary gaps, can alter the radial pressure profile, creating local pressure maxima that halt the inward drift of pebbles.

Our model includes a gap opened by a Jupiter-like planet in a fixed orbit at 5 au, a scenario that has been previously studied (e.g., S. J. Desch et al. 2018; P. Weber et al. 2018; T. Haugbølle et al. 2019; S. Jongejan et al. 2023; S. M. Stammler et al. 2023; T. Pfeil et al. 2025; E. Van Clepper et al. 2025). In reality, the gap may result from overlapping gaps formed by Jupiter and Saturn in resonance (A. Morbidelli & A. Crida 2007), or by a migrating Jupiter alone. Nevertheless, it is expected that the overall dust dynamics remain qualitatively consistent across these scenarios (see discussion in P. Weber et al. 2018). To mimic the presence of a Jupiter-like planet, we adopt the model from S. J. Desch et al. (2018) and S. Jongejan et al. (2023). We increase the α_{acc} value such as

$$\alpha' = \alpha_{acc} + (\alpha_{peak} - \alpha_{acc}) e^{-x^2}, \quad (4)$$

where $x = (r - r_J)/R_H$, with $R_H = r_J (M_J/3M_\odot)^{1/3}$ being the Hill radius of Jupiter. We start smoothly opening a gap from 0.6 Myr once the infall terminates, and linearly increase the value of α_{peak} to $1000\,\alpha_{acc}$ until 1.5 Myr. We use a simpler approach than S. J. Desch et al. (2018) and S. Jongejan et al. (2023), as our simulations of dust evolution begin 2 Myr after CAI formation and assume that Jupiter had already formed (see Section 2.2). Saturn is not included, although it is expected to have formed before disk dispersal. Previous studies showed that incorporating an additional Saturn-like planet does not necessarily inhibit the delivery of material to the outer region of Jupiter's gap (S. Jongejan et al. 2023). This depends on Saturn's formation history, and here we assume that Saturn did not perturb its vicinity significantly to affect dust evolution. All parameters employed to calculate gas evolution are listed in Table A1.

2.2. Dust Evolution Model

Some prior studies have investigated dust trapping with fixed particle sizes outside a planetary gap (S. J. Desch et al. 2018; S. Jongejan et al. 2023), distinguishing between large refractory inclusions and micrometer-sized matrix. These studies show that refractory inclusions are efficiently trapped in the pressure bump and that matrix crosses the gap, but in reality, different dust components are expected to collide and stick together, forming larger pebble-sized aggregates (E. Beitz et al. 2012; N. Machii et al. 2013; N. Gunkelmann et al. 2017; P. Umstätter & H. M. Urbassek 2021). If micrometer-sized matrix monomers grow to larger aggregates, the matrix comprises both small fragments that cross the gap and pebbles that remain trapped. Moreover, dust growth is typically necessary to reach pebble sizes large enough to aerodynamically decouple from the gas and initiate planetesimal formation (X.-N. Bai & J. M. Stone 2010; J. Lim et al. 2024). Other studies have modeled dust evolution using single-component dust growth

and fragmentation (S. M. Stammler et al. 2023; T. Pfeil et al. 2025; A. Houge et al. 2026), showing that while pebbles are trapped, fragmentation allows small dust to leak through the gap via advection and diffusion. These single-component models, however, are not directly applicable to the study of carbonaceous chondrite formation, because chondrules and refractory inclusions are coarser, more crystalline, and more resistant to fragmentation than the matrix (E. R. D. Scott & A. N. Krot 2014), and consequently, dust cannot be treated as a single component.

To fully account for these effects, we model collisions between different dust components and the more fragile nature of the matrix compared to refractory inclusions and chondrules. J. L. Hellmann et al. (2023) found that the abundance of refractory inclusions and chondrules in each carbonaceous chondrite group is correlated (except in CR chondrites, see Section 4), and suggests that the correlation may have been established before chondrule formation. Since our goal is to study the temporal variations in the abundances of refractory inclusions and chondrules over the matrix, for simplicity, we treat refractory inclusions and chondrules equally. We distinguish between two types of materials, fragile and rigid, which correspond to matrix and refractory inclusions/chondrules, respectively.

We model dust evolution using a two-dimensional Monte Carlo code that accounts for both dust transport and collisions (A. Zsom & C. P. Dullemond 2008; J. Drążkowska et al. 2013; V. Vaikundaraman et al. 2025). We compute the evolution of N_r representative particles, each representing N_i identical physical particles. We track the properties of each representative particle, including the particle mass m_i, spatial position (r_i, z_i), and composition (see the next section). Following A. Zsom & C. P. Dullemond (2008), each representative particle corresponds to a group of physical particles (or a "swarm") of constant total mass $M_{\rm swarm}$. Consequently, a representative particle i with particle mass m_i represents $N_i = M_{\rm swarm}/m_i$ physical particles. Each representative particle is subject to radial drift, advection, vertical settling, and diffusion, following the prescriptions in J. Drążkowska et al. (2013).

To calculate collisions between nearby particles, we build an adaptive grid every timestep (J. Drążkowska et al. 2013). The grid is divided into n_r radial and n_z vertical bins, resulting in a total of $n_r \times n_z$ cells. Each cell contains an equal number of representative particles. Collisions are computed only between representative particles within the same cell. For each representative particle i, the collision rate with a physical particle represented by particle j is given by

$$C_{i,j} = \frac{N_j,\ \Delta v_{i,j}\sigma_{i,j}}{V}, \tag{5}$$

where N_j is the number of physical particles represented by particle j, $\Delta v_{i,j}$ is the relative velocity between the particles, $\sigma_{i,j}$ is their geometric collision cross section, and V is the volume of the cell. Following a Monte Carlo approach, the time interval between collision events and the colliding particle pairs are determined by random sampling (D. T. Gillespie 1975). In each collision, a representative particle i interacts with a physical particle represented by j, and only particle i is updated after the interaction (A. Zsom & C. P. Dullemond 2008). Depending on their relative velocity $\Delta v_{i,j}$, the collision results in coagulation, fragmentation, or bouncing (see the next section).

When the particle size distribution is broad, collisions between particles i and j with very different masses may occur frequently, but a single collision changes the mass of the larger particle insignificantly. To speed up the Monte Carlo algorithm, we can approximate multiple physical collisions as a single effective collision. A. Zsom & C. P. Dullemond (2008) introduced a parameter, $dm_{\rm max}$, to group collisions between particles of very different masses. If the mass-ratio m_j/m_i is lower than $dm_{\rm max}$, the collision rate $C_{i,j}$ is then modified as follows:

$$C'_{i,j} = \frac{m_j/m_i}{dm_{\rm max}} C_{i,j}, \tag{6}$$

and if a collision happens, $\frac{m_i}{m_j} dm_{\rm max}$ particles of j collide with particle i. We set $dm_{\rm max} = 0.01$ as a fiducial value, which in local simulations introduces a mass error of 1%. However, in global disks, grouping collisions may be unrealistic if particles move across grid cells on timescales shorter than those required to complete the grouped collisions. To address this, we first estimate the maximum mass-ratio that allows for grouping in global disks by equating the dust transport timescale with the grouped collision timescale, which results in:

$$dm_{{\rm max},\,r} = \frac{\Delta r}{v_{r,i}} \frac{m_j}{m_i} C_{i,j}, \tag{7}$$

where Δr is the radial width of the grid cell. Here, the transport velocity $v_{r,i}$ accounts for all radial transport mechanisms except turbulence, which is excluded due to its stochastic nature. For the vertical transport, we replace the radial coordinate r by the vertical coordinate z. We define an adaptive grouping parameter, $dm'_{\rm max}$, which is the minimum between our fiducial value $dm_{\rm max}$ and the mass-ratio allowed for grouping in the global disk

$$dm'_{\rm max} = \min\left(0.01,\ dm_{\rm max,r},\ dm_{\rm max,z}\right). \tag{8}$$

This readjustment is especially important for studying dust evolution in a pressure bump, as overestimating particle growth leads to overestimating pebble trapping.

2.3. Collisions with Two Types of Material

Pebbles can consist of refractory inclusions and chondrules embedded in a matrix, forming chondritic aggregates. For each representative particle, we track the relative abundance of rigid (refractory inclusions/chondrules) and fragile (matrix) material. The corresponding rigid mass fraction of particle i is defined as:

$$f_i^{(d)} = \frac{m_{{\rm rigid},i}}{m_i}, \tag{9}$$

where $m_{{\rm rigid},i}$ and m_i are the mass of rigid components and the total mass of the particle. The superscript d in $f_i^{(d)}$ indicates that the property is dynamic and is updated in every collision. Assuming that the fragile and rigid materials have internal densities of $\rho_{\rm fragile} = 1.2\,{\rm g\,cm^{-3}}$ and $\rho_{\rm rigid} = 3.3\,{\rm g\,cm^{-3}}$ (J. L. Hellmann et al. 2020), the internal density of the particle

is calculated as:

$$\rho_i = \left(\frac{f_i^{(d)}}{\rho_{\rm rigid}} + \frac{1 - f_i^{(d)}}{\rho_{\rm fragile}} \right)^{-1} . \quad (10)$$

If representative particle i collides with a physical particle j at a relative velocity Δv_{ij} lower than the fragmentation threshold $v_{\rm frag}$, and if at least one of the particles contains matrix material, we assume that the two particles stick together. During a sticky collision, the rigid mass fraction of particle i is updated as follows:

$$f_i^{(d)} = \frac{f_i^{(d)} m_i + f_j^{(d)} m_j}{m_i + m_j} . \quad (11)$$

We assume that at typical relative velocities in the disk midplane (>mm s^{-1}), two purely rigid particles always bounce when they collide (N. Gunkelmann et al. 2017).

By tracking only the dynamic fraction $f_i^{(d)}$ of two types of material, the Monte Carlo method presented by A. Zsom & C. P. Dullemond (2008) does not guarantee the conservation of the total mass for rigid and fragile material because we only update representative particle i when particle i and j collide (see discussion in S. Krijt et al. 2016; A. Houge & S. Krijt 2023). This can lead to fluctuations that can grow over time. To address this issue, we introduce static properties for each particle, which specify the type of material to be tracked in a disruptive collision. We define two key properties: $f_i^{(s)}$ and $m_{{\rm rigid},i}^{(s)}$. Here, the superscript s denotes a static property. If a traced particle is initialized with $f_i^{(s)} = 1$, it requires a corresponding mass value $m_{{\rm rigid},i}^{(s)}$, which is assigned according to a power-law distribution (see Section 2.4). Throughout the evolution of particle i, we consistently track a rigid particle of mass $m_{{\rm rigid},i}^{(s)}$. This rigid particle may be embedded within a larger chondritic aggregate containing both types of material. In a disruptive collision, if the tracked fragment cannot retain the rigid monomer of mass $m_{{\rm rigid},i}^{(s)}$, we always choose to track the rigid monomer. Conversely, if $f_i^{(s)} = 0$, we track a particle that contains at least one fragile monomer. To ensure the same threshold for separating material regardless of the particle's $f_i^{(s)}$ value, we track a purely fragile particle when the fragment cannot retain a rigid particle of mass $m_{{\rm rigid},i}^{(s)}$. Therefore, if a particle has $f_i^{(s)} = 0$, the static mass $m_{{\rm rigid},i}^{(s)}$ is updated whenever the particle collides with a physical particle of similar mass (within 90%) that has $f_i^{(s)} = 1$. Fragmentation events correct the fluctuations that arise during coagulation. As a result, when the particle size distribution is limited by fragmentation, as in a pressure bump, the dynamic properties fluctuate around their average static values. In this way, fluctuations do not grow over time and decrease with increasing numerical resolution (see Figure B1).

When representative particle i collides with a physical particle j at a relative velocity $\Delta v_{ij} > v_{\rm frag}$ and particle i contains matrix material, we assume that particle i fragments. The mass of particle i is distributed into fragments following a power-law distribution, and the size of the fragment to be tracked is then selected from the distribution:

$$m_i' = (\chi \cdot (m_i^{\kappa} - m_0^{\kappa}) + m_0^{\kappa})^{1/\kappa}, \quad (12)$$

where $\kappa = 1/6$ (J. S. Dohnanyi 1969), m_0 is the mass of a fragile monomer of 1 μm in radius, χ is a random number drawn from a uniform distribution, and m_i' is the mass of particle i after the disruptive collision. We then check if the static rigid monomer in the aggregate ($m_{{\rm rigid},i}^{(s)}$) could be retained in that fragment of mass m_i'. If so, we update the mass while keeping $f_i^{(d)}$ constant. This approach is motivated by simulations showing that the chondrules tend to remain in the largest fragments (P. Umstätter & H. M. Urbassek 2021). If the rigid monomer cannot be retained, we check the static property $f_i^{(s)}$. If $f_i^{(s)} = 1$, we trace a rigid particle with mass $m_{{\rm rigid},i}^{(s)}$. If $f_i^{(s)} = 0$, we trace a fragile particle. We select the mass of the fragile fragment from the power-law distribution in Equation (12), but replacing m_i with $m_{{\rm rigid,i}}^{(s)}/f_i^{(d)}$. After choosing the tracked fragment, the dynamic fraction is also updated accordingly.

Laboratory experiments reported a fragmentation velocity threshold of 1 m s^{-1} (C. Güttler et al. 2010). However, these experiments were conducted with a single material composed of micron-sized monomers. Alternative laboratory experiments with rigid and fragile materials, as well as granular mechanics simulations, have shown that growth is enhanced when both materials are combined (E. Beitz et al. 2012; N. Gunkelmann et al. 2017). The fragmentation velocity of chondritic aggregates remains uncertain. We assume a constant fragmentation threshold of $v_{\rm frag} = 2$ m s^{-1}, both for the reason mentioned earlier and because the Stokes number (St; a parameter describing the dust response to aerodynamic drag), limited by fragmentation in a pressure bump, must exceed 0.01 to trigger planetesimal formation (X.-N. Bai & J. M. Stone 2010), which is not possible in our models if we set $v_{\rm frag} = 1$ m s^{-1}. We assume that rigid components survive without fragmenting to collisional velocities driven by typical nebular conditions, such as turbulence. Although chondrule fragments are present in chondrites (E. R. D. Scott & A. N. Krot 2014), most chondrules are preserved as near-spherical igneous droplets. The presence of fragments may reflect energetic events, such as nebular shocks, which can generate collision velocities high enough to fragment chondrules (e.g., F. J. Ciesla 2006; E. Jacquet & C. Thompson 2014; S. Arakawa & T. Nakamoto 2019). Such events are not included in our model.

Matrix in chondrites is commonly found as fine-grained rims surrounding chondrules and refractory inclusions, as well as interstitial material between them (e.g., E. R. D. Scott & A. N. Krot 2014; S. B. Simon & L. Grossman 2015). C. W. Ormel et al. (2008) showed that micrometer-sized matrix material can first stick to chondrules to form porous rims, and that subsequent collisions lead to rim compaction. Afterward, rimmed chondrules may collide and stick with other rimmed chondrules. In contrast, collisions between rimmed chondrules at relative velocities on the order of m s^{-1} can lead to ejection of rims (P. Umstätter et al. 2019). Within dust traps, collisions between small matrix and rigid monomers are frequent, and dust collides at relative velocities reaching up to $\sim$2 m s^{-1} for our disk parameters. Under such conditions, chondrule (and potentially refractory inclusion) rims are likely to form and be disrupted continuously within the same pressure bump. Therefore, we simplify the model by assuming perfect sticking between rigid components and matrix material at collision velocities below 2 m s^{-1}.

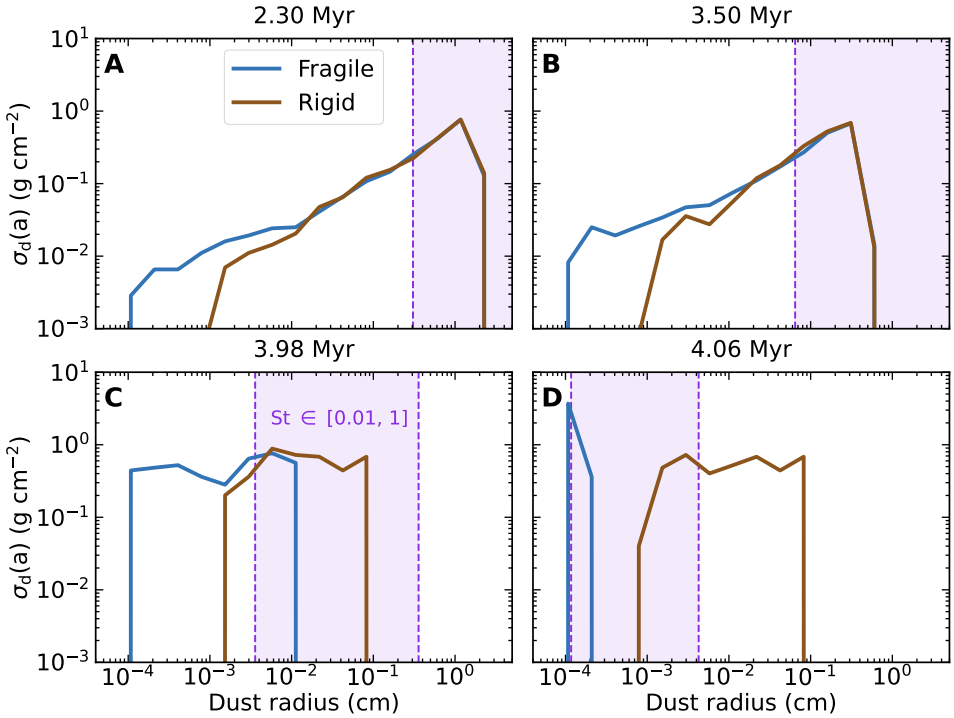

Figure 3. Particle size distribution from solely collisional evolution of fragile and rigid material at different stages of disk evolution in a zero-dimensional simulation. The surface density is computed on a logarithmic scale σ_d (see Equation 13). Panels (A) and (B) show time-averaged results over 50 snapshots, while panels (C) and (D) represent single-time snapshots. The total mass is equally distributed between 200 fragile and rigid particles. Rigid monomer radii range from 10 to 1000 μm, while fragile monomers are 1 μm. The purple dashed lines delimit the domain of interest for planetesimal formation, for pebbles with Stokes numbers (St) between 0.01 and 1 for an internal density of 1.76 g cm^{-3} (corresponding to a rigid mass fraction of 0.5), except in panel (D), where the rigid mass fractions are 0 and 1 for Stokes numbers of 0.01 and 1, respectively. St = 1 line is not displayed in panels (A) and (B) because it corresponds to particle sizes larger than those shown. (A)–(C) The maximum aggregate size of combined fragile and rigid material decreases over time due to ongoing fragmentation. (D) At the latest stages, the chondritic aggregates are fragmented into their constituent components.

2.4. Size Distribution from Zero-dimensional Simulations

We first conduct a zero-dimensional Monte Carlo simulation to analyze the effect of gas removal on the particle size distribution when incorporating the new fragmentation model. The results are presented in Section 3.1. We compute the collisional evolution of a single grid cell with 200 particles in the dust trap, which, for the fiducial disk parameters at 2 Myr, is located at 6.1 au. We assume a vertically integrated dust-to-gas ratio of 0.05 for this simulation. This metallicity is consistent with the value expected to trigger planetesimal formation for the Stokes number St = 0.01 (Equation 18).

We initialize particles using a power-law size distribution consistent with fragmentation-limited dust growth, $n(a) \propto a^{-3.5}$ (T. Birnstiel 2024), which is later stabilized by the simulation. We randomly choose half of the particles to have $f_{s,rigid} = 1$. We determine the mass of the rigid monomer ($m_{s,rigid}$) from the power-law distribution $n(a) \propto a^{\zeta}$, assuming spherical monomers with radii a. We took 10 μm and 1000 μm as the minimum and maximum sizes of the distribution, and a power index of $\zeta = -3.9$, resulting in a mean radius of 230 μm. These values cover the typical sizes of CAIs and chondrules (R. H. Jones 2012; E. T. Dunham et al. 2023).

After initializing the static properties, we select particle masses from the fragmentation-limited power-law distribution. We then check whether a particle of the chosen size could retain 50% of its mass in rigid monomers. If this condition is met, the particle is initialized with $f_{d,rigid} = 0.5$. For particles that are too small to contain rigid monomers, when $f_{s,rigid} = 0$, the particles are chosen to be pure fragile with the previously chosen mass. Otherwise, if $f_{s,rigid} = 1$, the particle is initialized as a rigid monomer with mass $m_{s,rigid}$.

To illustrate the particle size distribution, in Figure 3 we compute the surface density on a logarithmic scale as

$$\sigma_d(a) = N(a)m(a)a, \tag{13}$$

where a is the radius of dust particles, m is the particle mass, and N is the number of particles with the corresponding radius (T. Birnstiel 2024).

2.5. Global Simulations of Dust Evolution

We then perform simulations that include dust collisional evolution, transport, and planetesimal formation. Due to the high computational demand of the Monte Carlo simulations, we divide our simulations into two parts. We first ran a global dust evolution simulation, starting at 2 Myr after CAI formation, to model the delivery of pebbles to the dust trap. We compute the collisional evolution and transport in the outer regions of the disk ($r > 6.5$ au). Later, we use the output of this simulation to calculate the pebble flux at 6.5 au in a local simulation of the outer gap edge (see next section).

We assume an integrated dust-to-gas ratio of $Z_0 = 5 \cdot 10^{-5}$ across a 2 Myr-old disk, corresponding to a total dust mass of approximately 1.2 Earth masses. This estimate aligns with the low dust masses observed in Class II disks (M. Ansdell et al. 2016). We initialize the particle size distribution similarly to the previous zero-dimensional simulations. However, instead of assuming a uniform abundance of rigid material, we decrease the rigid abundance with radial distance. Assuming

that the largest rigid particles carry most of the rigid mass, their decreasing abundance with radial distance is consistent with dust evolution models, which predict that millimeter-sized grains undergo significant radial drift before 2 Myr in the outer disk. On the other hand, because we adopt a size distribution for the rigid monomers (ranging from 10 μm to 1 mm) and allow the matrix to grow into large pebbles, the reduction of rigid abundance in the outer disk is expected to be less pronounced than in models that assume fixed particle sizes and millimeter-sized refractory inclusions (e.g., S. J. Desch et al. 2018; S. Jongejan et al. 2023).

To model the initial decrease of rigid particles with distance, we first set an initial value of $\bar{f}_{\rm rigid}$, and then the value is modified by multiplying it by:

$$p_{\rm rigid} = \frac{(a_{\rm ri,lim})^{\zeta+4} - (a_{\rm rigid}^{\rm min})^{\zeta+4}}{(a_{\rm rigid}^{\rm max})^{\zeta+4} - (a_{\rm rigid}^{\rm min})^{\zeta+4}}, \quad (14)$$

where $a_{\rm ri,lim}$ is the size limited by fragmentation or radial drift, assuming the Epstein regime (T. Birnstiel 2024), given by:

$$a_{\rm ri,lim} = \frac{2}{\pi}\frac{\Sigma_{\rm g}{\rm St}_{\rm lim}}{\rho_{\rm rigid}}, \quad (15)$$

and $a_{\rm rigid}^{\rm min}$ is 10 μm and $a_{\rm rigid}^{\rm max}$ is the minimum value between 1000 μm and $a_{\rm ri,lim}$. ${\rm St}_{\rm lim}$ is the Stokes number limited by fragmentation or radial drift (T. Birnstiel et al. 2012), and therefore the minimum value between

$${\rm St}_{\rm frag} = \frac{0.37}{3\alpha_{\rm t}}\left(\frac{v_{\rm frag}}{c_{\rm s}}\right)^2, \quad (16)$$

$${\rm St}_{\rm drift} = \frac{1}{2}\frac{v_{\rm K}}{\Delta v}Z_0, \quad (17)$$

where $v_{\rm K}$ is the Keplerian velocity and Δv is the deviation from the Keplerian rotation of the gas (see Equation (3)). In regions where dust growth is limited by the drift barrier (Equation 17), the initial particle size distribution follows $n(a) \propto a^{-2.5}$ (T. Birnstiel 2024). The probability of initiating a rigid particle is then given by $\bar{f}_{\rm rigid} \times p_{\rm rigid}$, and the dynamic rigid mass fraction of particles ($f_{\rm d,rigid}$) is set to the same value as this corrected probability. The abundance of rigid material in the solar system's protoplanetary disk is uncertain. We set $\bar{f}_{\rm rigid} = 0.5$, resulting in an overall rigid disk mass of 0.3 Earth masses, approximately 25% of the total dust mass, and an average rigid monomer radius of 260 μm. These values decrease with distance from the Sun; for instance, beyond 50 au, the overall rigid disk mass drops to ~15%, with an average rigid monomer radius of 45 μm. With this assumption, our results are consistent with meteorite constraints (see Section 4). More importantly, the dynamical processes we identify in this work are independent of this choice.

We simulate 80 radial and 40 vertical grid bins, each cell containing 200 particles. No feedback from local to global simulations is included; once particles cross the inner boundary of the global simulation, they are no longer tracked. To stabilize the collisional model, we first perform 100 iterations without transport. Then, we simulate dust evolution until the gas disk dissipates, approximately 4.2 Myr after CAI formation (see Figure 2). The output of this simulation is later used as the source of a more localized simulation. All parameters employed to calculate dust evolution are listed in Table A2.

2.6. Local Simulation with Planetesimal Formation

We simulate dust evolution at the outer edge of the gap with a resolution high enough to resolve planetesimal formation. For this setup, we chose an inner boundary of 5.725 au to resolve collisions, as particles that cross this location commonly leak through the gap without colliding due to their high radial velocities driven by advection. We set the outer boundary at 6.5 au for a dust trap located at 6.1 au.

We employ a grid with 28 radial and 28 vertical cells, with each cell containing 200 particles, as the simulation converges for this resolution. Particles are introduced at 6.5 au from the output of the global simulation, while some particles are lost as they pass through the gap. As the simulation progresses, the number of particles naturally would increase, making it computationally challenging to extend the run until 4.2 Myr. To address this issue, we maintain a constant number of particles throughout the simulation. Then, the total mass of each representative particle ($M_{\rm swarm}$), which is the same for all particles, changes over time. We randomly remove or duplicate particles as needed to keep the number of particles constant. This approach allows us to extend the simulation over long timescales without increasing computational costs at later times. We validate our results by running the simulation multiple times with the same initial conditions and confirming their consistency.

We implement a simple criterion for simulating planetesimal formation by the streaming instability (SI). If the integrated pebble-to-gas ratio exceeds $Z_{\rm crit}$ from J. Lim et al. (2024; their Equation (19)),

$$\log Z_{\rm crit} = 0.15\log^2(\alpha_{\rm t}) - 0.24\log({\rm St})\log(\alpha_{\rm t}) - 1.48\log({\rm St}) + 1.18\log(\alpha_{\rm t}), \quad (18)$$

we trigger planetesimal formation. This expression was derived for pebbles with a single Stokes number in the range $0.01 \leqslant {\rm St} \leqslant 0.1$, whereas our simulations include particle size distribution. For our fiducial parameters, the Stokes number limited by fragmentation is near 0.02 (Equation (16)). To calculate the critical metallicity for SI, we select the lower value of ${\rm St} = 0.01$, which, together with $\alpha_{\rm t} = 10^{-4}$, yields a value of $Z_{\rm crit} = 0.05$. As the gas disperses, rigid particles acquire Stokes numbers that exceed the fragmentation limit (see Section 3.1). While we expect that pebbles with ${\rm St} > 0.1$ can still form planetesimals, the upper Stokes number limit remains uncertain. We set this limit at ${\rm St} = 1$, beyond which solids no longer behave as pebbles. Nevertheless, particles that trigger the SI remain below a Stokes number of 0.1 throughout our simulations.

If the criterion for forming planetesimals is fulfilled, we compute the number of representative particles converted into planetesimals during the timestep dt following:

$$N_{\rm plt} = \zeta_{\rm eff}\frac{N_{\rm swarm}({\rm St} > {\rm St}_{\rm crit})}{T_{\rm K}}dt, \quad (19)$$

where $T_{\rm K}$ is the orbital period and $\zeta_{\rm eff}$ denotes the planetesimal formation efficiency (J. Drążkowska et al. 2016). We adopt a fiducial value of $\zeta_{\rm eff} = 10^{-3}$ (J. B. Simon et al. 2016). We assume that the planetesimals have the same composition as their pebble precursors.

3. Results

3.1. Collisional Evolution of Dust with Different Fragility

To understand how including fragile and rigid particles affects dust evolution, we first perform a zero-dimensional simulation, in which we distribute half of the material as fragile and the other half as rigid monomers. Fragile material is composed of monomers with radii of 1 μm and a density of 1.2 g cm^{-3}, whereas rigid monomers have radii ranging from 10 to 1000 μm and are characterized by a higher density of 3.3 g cm^{-3}. All dust particles stick to each other upon collision if the impact velocity remains below the fragmentation threshold of 2 m s^{-1}, except for collisions between rigid monomers, which result in bouncing (see Section 2.3 for details of the fragmentation model and Section 2.4 for a description of the numerical implementation).

When the dust grows to centimeter- and millimeter-sized chondritic aggregates (Figures 3(A) and (B)), the largest pebbles are composed of rigid and fragile material equally. Most pebbles have Stokes numbers between 0.01 and 1, and thereby can trigger planetesimal formation by the SI if the pebble-to-gas ratio is high enough. When the gas surface density decreases significantly by photoevaporation, the sizes at which aggregates containing both fragile and rigid material shift to submillimeter sizes (Figure 3(C)). At the same time, larger rigid particles remain as monomers with Stokes numbers larger than 0.01. When the gas disk depletes even further (Figure 3(D)), many of the rigid monomers are too large to trigger planetesimal formation (St $>$ 1), while the Stokes numbers of matrix particles lie in the optimal range for planetesimal formation. These results will be important for understanding the late formation of the CR and CI chondrite parent bodies in the next section.

3.2. Dust Evolution Across the Disk

While the simulation described above highlights the critical role of the gas evolution in shaping the dust size distribution, a realistic model must also account for dust filtering, material delivery from outer regions, and planetesimal formation. To model how the dust population in the disk evolved in time and space, we ran a global simulation of the outer disk. The radial drift velocity of particles scales with their Stokes number, which increases with particle size and in regions of lower gas density, such as the outer disk (T. Birnstiel 2024). As a result, millimeter-sized rigid particles in the outer-disk drift inward on timescales shorter than a Myr. To initialize a Class II disk, we reduce the dust-to-gas ratio and the abundance of large rigid monomers in the outer disk to reflect their earlier rapid inward drift (see Section 2.5). This results in an outer disk that is relatively enriched in fragile material (i.e., fine-grained matrix). We then run a high-resolution local simulation at the outer edge of the gap (see Section 2.6). When the conditions for planetesimal formation are satisfied, we remove the pebbles that became part of planetesimals and assume that these planetesimals inherit the same rigid mass fraction as their pebble precursors.

Figure 4 shows the dust evolution in the disk for rigid and fragile materials. Initially, these materials are equally distributed across the disk (Figure 4(A)), except in the outer disk, where, as noted above, the abundance of rigid material is reduced due to the fast radial drift of large rigid monomers. By 2.3 Myr, pebble trapping at the outer edge of the gap increases the dust density around 6.1 au for both rigid and fragile material (Figure 4(B)), but the increase is higher for rigid than for fragile material. This is because collisions between aggregates are frequent in the dust trap, and high-velocity impacts tend to fragment fragile aggregates more efficiently into smaller dust particles. These smaller fragments are more strongly coupled to the gas and can leak through the gap, while the larger and denser rigid monomers remain trapped. At around 2.3 Myr, the total dust surface density exceeds the threshold for triggering planetesimal formation (Figure 4(B)). By 3.5 Myr, the dust surface density from rigid material has decreased significantly with respect to that of the fragile material (Figure 4(C)). This decrease is primarily due to a temporal reduction in the number of rigid particles delivered to the dust trap while planetesimal formation regulates the dust amount in the trap (see Figure B2). While pebbles are incorporated into planetesimals over time, the dust trap is replenished by material that drifts from the outer regions. By this time, submillimeter-sized rigid particles, which are the main carriers of the total rigid mass, have already drifted into the dust trap. As a result, the dust population is now replenished mainly by fragile matrix-like material. Consequently, the differences in dust filtering and delivery rates of rigid and fragile material can account for the low abundance of matrix in early-formed carbonaceous chondrites and the increase in matrix in later-formed ones.

At the later stage of disk evolution, at around 4 Myr, photoevaporation begins to widen the existing gap (see Figure 2). As gas is expelled from this region, the surrounding gas attempts to refill the gap, increasing the gas velocity near the outer edge of the gap. Micrometer-sized fragile particles, which remain well coupled to the gas, move along with the gas in an effort to refill the gap. As a result, they are carried away from the planetesimal formation region (Figure 5(A)). In contrast, rigid monomers, which are denser and larger, are efficiently trapped in the dust trap (Figure 5(A)) and have high Stokes numbers (Figure 3(C)). This increases the ratio of rigid-to-fragile material at the outer edge of the gap (Figure 5(A)). If sufficient similar-sized rigid particles are present, they can form planetesimals composed of matrix-poor dust, reminiscent of the CR chondrites. At even later times (Figure 5(B)), the gap widens, and the gas density decreases further. By this point, most rigid particles have either been incorporated into planetesimals or transported outward. Simultaneously, the smallest fragile monomers begin to accumulate in the trap, leading to the formation of planetesimals made primarily of matrix, such as the CI chondrites. Together, these results show that photoevaporation can lead to the late formation of matrix-poor planetesimals from mostly rigid monomers, followed by the formation of matrix-rich planetesimals.

4. Discussion

4.1. Prolonged Carbonaceous Chondrite Formation in a Single Pressure Bump

The key observation from our results is that they fully reproduce the observed compositional range of carbonaceous chondrite parent bodies over time. This is illustrated in Figure 6, where we show the temporal evolution of the matrix mass fraction of planetesimals and pebbles in the dust trap from our model compared to the observed ages and compositions of carbonaceous chondrites. Pebbles start with

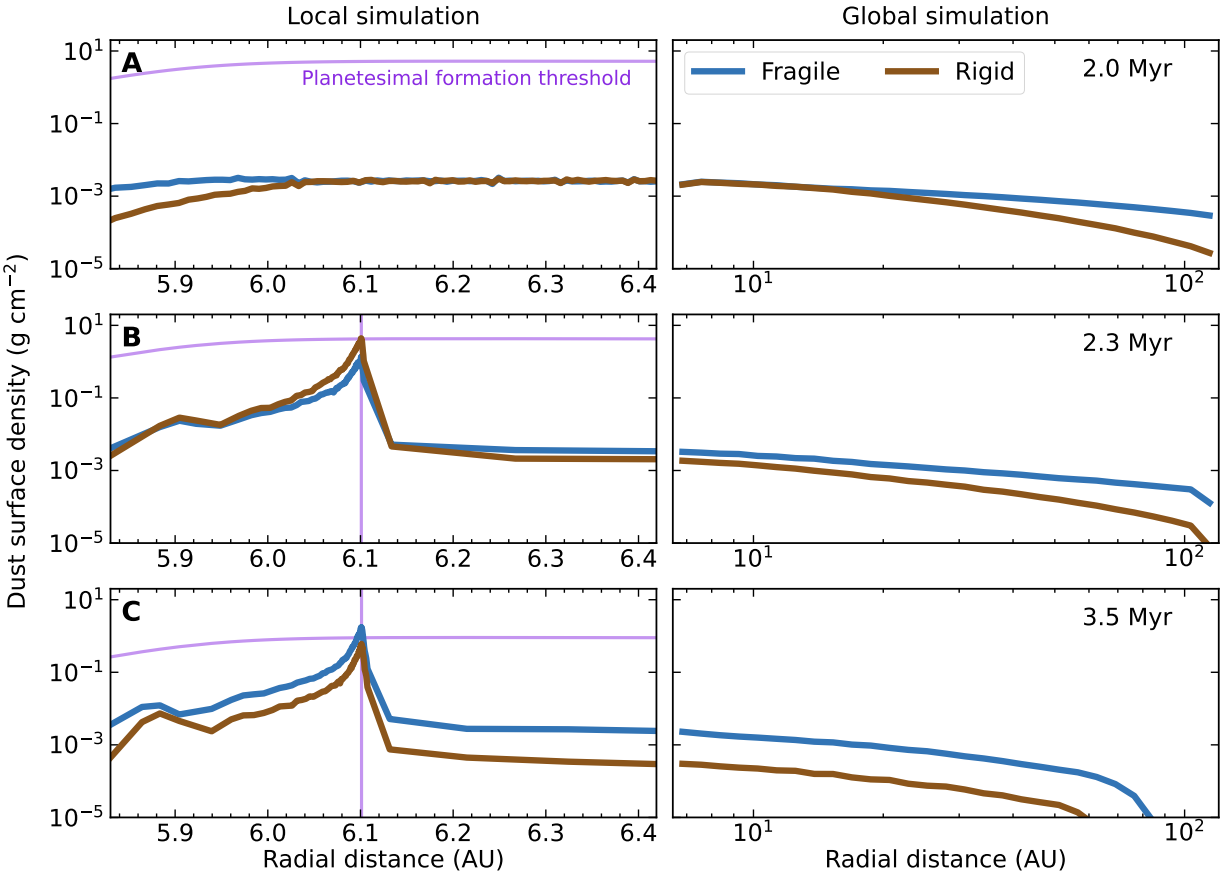

Figure 4. Dust surface density evolution across the disk. Local and global simulations are shown together at different snapshots. (A) Start of the simulation at 2 Myr. Dust is distributed equally between rigid and fragile material, except when restricted by the radial drift barrier. The purple (nearly) horizontal line indicates the minimum dust surface density required for planetesimal formation. (B) Simulation at 2.3 Myr. The dust surface density in the dust trap increases, particularly for rigid material, due to the leakage of fragile material. The purple vertical line indicates the location where planetesimals form at approximately 6.1 au. (C) Simulation at 3.5 Myr. The surface density of rigid material in the trap decreases as the material replenishing the dust trap is matrix-rich.

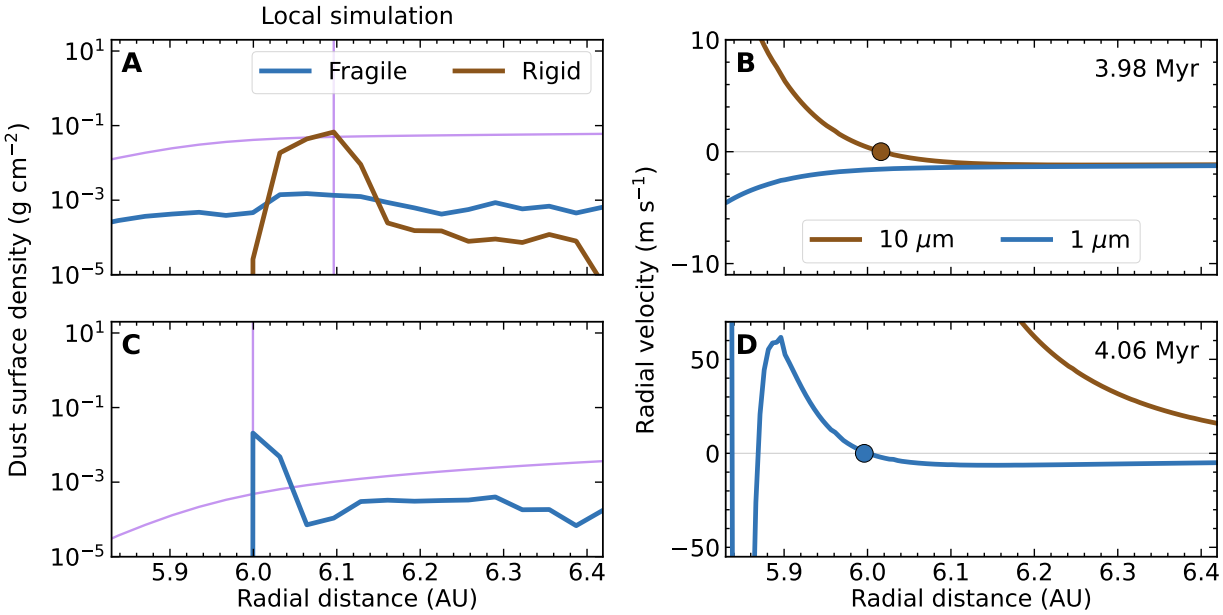

Figure 5. Dust evolution at the outer edge of the gap during the gap-widening phase driven by photoevaporation. (A) Dust surface density at 3.98 Myr. The purple (nearly) horizontal line indicates the minimum dust surface density required for planetesimal formation, and the vertical one the location where this threshold is exceeded. (B) Radial velocities of the smallest rigid and fragile monomers at 3.98 Myr. The dot at around 6 au denotes the location where the smallest monomers of each material get trapped, corresponding to where their radial velocity is zero. At this time, small matrix fragments leak through the gap along with the gas flow, while all rigid particles remain trapped. (C) Dust surface density and (D) radial velocities at 4.06 Myr. By this time, rigid monomers have been pushed outward by the expanding gap, while the smallest matrix monomers are now trapped near 6 au. This sequence explains the dynamics during the formation of matrix-poor planetesimals and the subsequent formation of matrix-rich ones.

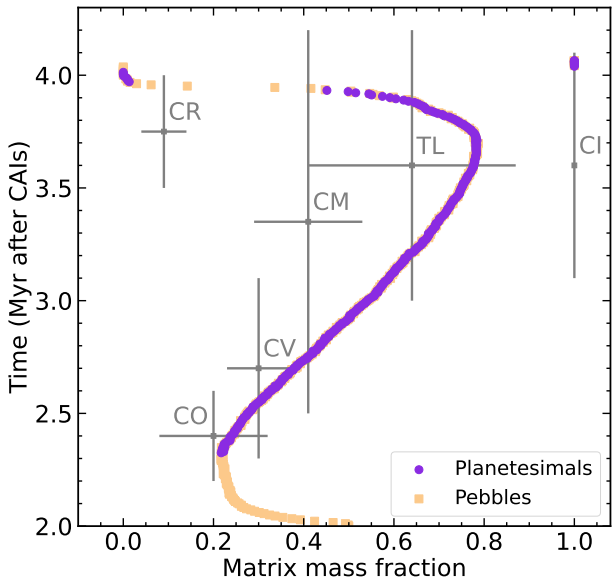

Figure 6. Matrix mass fraction in planetesimals depending on their formation time. Planetesimals are indicated with purple dots, and the largest pebbles in the dust trap (with Stokes numbers between 0.01 and 1) with orange squares. Meteoritic data represented with gray points with error bars are from J. L. Hellmann et al. (2023) and references therein.

an assumed average matrix mass fraction of 50% at 2 Myr. This fraction initially decreases due to the loss of the matrix passing through the gap, which halts at a matrix fraction of around 20% at ∼2.3 Myr. At this point, the conditions for planetesimal formation are met for the first time, reproducing the accretion age and composition of the Ornans- (CO) and Vigarano-type (CV) chondrites. Since the dust delivered from the outer disk is more matrix-rich, the matrix fraction of pebbles and planetesimals increases until ∼3.8 Myr, reproducing the properties of the more matrix-rich Mighei-type (CM) chondrites and the ungrouped Tagish Lake (TL) chondrite. It is important to note that incorporating multicomponent dust evolution and planetesimal formation, as in this study, is required to quantify this temporal increase of matrix in the pressure bump (see Figure B2). By contrast, previous studies that did not consider dust growth and planetesimal formation have shown that the abundance of refractory inclusions in the pressure bump increases over time (S. J. Desch et al. (2018), their Figure 8; and S. Jongejan et al. (2023) their Figure 17), which is contrary to the observations among carbonaceous chondrites.

As the protoplanetary disk approached its dispersal, the last phase of planetesimal formation occurred in two stages: first, remnant rigid particles formed CR-like planetesimals and, later, the smaller, less dense, fragile grains formed CI-like planetesimals (Figure 5). In the first stage, the matrix abundance in the largest pebbles and planetesimals rapidly decreases due to the gap widening during photoevaporation (Figures 5(A) and (B)) and, as such, can reproduce the very low abundance of matrix in the CR chondrites. Forming CR-like planetesimals in this manner requires that enough rigid particles remained at around 4 Myr for a local pebble-to-gas ratio high enough for planetesimal formation. Our simulations reproduce this scenario, forming matrix-poor bodies, but we also found scenarios in which planetesimal formation is not triggered due to the scarcity of rigid particles at a later stage (see Figure B3). However, these scenarios can still explain the formation of CR chondrites if a later generation of chondrules formed, supplying the rigid material required for planetesimal formation. This interpretation is consistent with the distinctive composition of CR chondrites, which are rich in late-formed chondrules but poor in refractory inclusions (G. Budde et al. 2018; J. F. J. Bryson & G. A. Brennecka 2021; Y. Marrocchi et al. 2022).

Like the CR chondrites, CI chondrite-like planetesimals also form late, and our results suggest their formation times differ by less than 0.1 Myr (Figures 5 and 6). The CI chondrites form when only micrometer-sized fragile particles are trapped and meet the criteria for planetesimal formation (Figures 5(C) and (D)), reproducing the high matrix abundance of these carbonaceous chondrites. In our model, planetesimal formation is only monitored at the outer gap edge of the local simulation, but we expect that matrix-rich planetesimals continue to form across the outer disk as the gap expands (D. Carrera et al. 2017; B. Ercolano et al. 2017). The CI chondrites are isotopically distinct, in particular for Fe and Ni, which has been suggested to reflect either formation in a spatially separated region of the disk (T. Hopp et al. 2022) or fractionation of isotopically anomalous FeNi metal grains during carbonaceous chondrite formation (F. Spitzer et al. 2024). Although FeNi metal grains have not been included in our model, our findings point toward the latter scenario because they show that CI chondrite-like objects can form in the same disk region and from the same starting materials as other carbonaceous chondrites.

In our fiducial simulation, the total mass of planetesimals formed in the pressure bump is approximately 0.5 Earth masses. Most of the planetesimals are compositionally similar to CO, CV, CM, or TL (∼99.2%; see Figure B4), and CR-like and CI-like planetesimals are significantly less abundant (∼0.6% and 0.2%, respectively). However, these fractions vary under additional considerations. Including late-generation chondrule formation (i.e., the aforementioned supply of rigid material at late stages) may increase the CR fraction. In addition, tracking planetesimal formation across the outer disk as the gap opens raises the CI fraction to ∼5%. Additional refinements in the model, such as adopting a more extended and massive outer disk, would further increase the CI fraction. More work is required to assess whether the mass distribution of carbonaceous chondrite parent bodies predicted by our model is consistent with current observational constraints. On the one hand, the fraction of the formed planetesimals that is later implanted into the asteroid belt, the main source of meteorites (F. Colas et al. 2020), should be quantified. On the other hand, meteorite collections alone almost certainly do not provide a representative sample of parent body abundances. Notably, although CI chondrites are rare among meteorite falls on Earth, JAXA's Hayabusa2 mission to asteroid Ryugu and NASA's OSIRIS-REx mission to asteroid Bennu revealed that these two asteroids are CI-like (T. Yokoyama et al. 2023; D. S. Lauretta et al. 2024; J. J. Barnes et al. 2025), suggesting that this planetesimal group may be more common than inferred from meteorite collections.

In summary, our results show that although carbonaceous chondrites are compositionally distinct and formed over an extended period of time, they can all have formed in a single long-lived dust trap of the disk. If instead photoevaporation were the sole mechanism for enhancing the local pebble-to-gas ratio, planetesimal formation would first occur in the outer disk beyond 100 au (D. Carrera et al. 2017, their Figures 6 and 7). These outer-disk planetesimals would be expected to be

matrix-rich, as radial drift depletes this region of refractory inclusions and chondrules. Subsequent inside-out photoevaporation could then generate planetesimals at smaller heliocentric distances, but only within a narrow time interval of ∼0.1 Myr (D. Carrera et al. 2017), with compositions likely similar to those of CI chondrites (Figure 5). All these predictions are inconsistent with the prolonged period of formation of compositionally distinct bodies as recorded in the carbonaceous chondrites (J. L. Hellmann et al. 2023). Our results, therefore, show that a long-lived pressure bump provides a more plausible explanation for the temporal and compositional diversity of carbonaceous chondrites than photoevaporation alone.

4.2. Implications for Early Planetesimal Formation in the Outer Disk

Although our model is devised to examine the formation of carbonaceous chondrites, our results also have implications for understanding earlier planetesimal formation in the outer disk. Iron meteorites sample the metal cores of differentiated planetesimals and, based on their Hf-W core formation ages, are thought to have formed within the first Myr of the solar system (T. Kleine et al. 2005; T. S. Kruijer et al. 2014). Thus, iron meteorites represent an earlier generation of planetesimals than the carbonaceous chondrites. Among these irons, the carbonaceous chondrite (CC)-type irons have isotopic compositions similar to those of the carbonaceous chondrites and, therefore, appear to have formed from the same precursor materials as the carbonaceous chondrites (T. S. Kruijer et al. 2017). Based on their isotopic compositions, it has been argued that CC irons, like the matrix-poor carbonaceous chondrites, are enriched in refractory inclusions and chondrules, while irons with CI chondrite-like isotopic compositions do not seem to exist (F. Spitzer et al. 2025). Combined with the results of our model, this suggests that the CC irons, like the carbonaceous chondrites, formed in a dust trap, indicating that such substructures in the disk already existed earlier than modeled here. Importantly, the lack of irons with CI chondrite-like isotopic compositions is consistent with this interpretation, because, as noted above, CI chondrites only formed at the end of the disk's lifetime, when photoevaporation enhanced the pebble-to-gas ratio and allowed the accretion of micrometer-sized dust components. Since the CC irons formed much earlier, several Myr before photoevaporation occurred, these objects cannot have acquired a CI chondrite-like isotopic composition.

Several other CC iron meteorites exhibit CR chondrite–like isotopic compositions (F. Spitzer et al. 2025). As argued above, like for the CI chondrites, photoevaporation may have been important in the formation of the CR chondrites, raising the question of how objects with a CR-like isotopic composition can also have formed early, several Myr before photoevaporation commenced. It has been proposed that CR chondrites formed from matrix-rich precursor material, which has been converted into chondrules prior to CR chondrite parent body accretion (Y. Marrocchi et al. 2022). Thus, one possibility is that some CC irons acquired a CR-like isotopic composition by accreting this material predominantly as matrix-rich pebbles. As such, early-formed planetesimals may have undergone an independent sequence of matrix accumulation over time in a substructure (analogous to the progressive matrix increase illustrated in Figure 4(C)). This hypothesized substructure, however, does not necessarily originate from a fully formed Jupiter (R. Brasser & S. J. Mojzsis 2020; A. Morbidelli et al. 2024). At earlier times, when the global dust-to-gas ratio was higher, even smaller pressure bumps could have accumulated enough material to trigger planetesimal formation. This pressure bump could have triggered Jupiter's formation (T. C. H. Lau et al. 2024), thus explaining the observed prolonged separation of carbonaceous and noncarbonaceous (NC) reservoirs.

4.3. Implications for the Formation of NC Chondrites

Substructures are common in protoplanetary disks (S. M. Andrews et al. 2018), and a single planet can create multiple pressure bumps in its inner regions (E. Lega et al. 2025; B. Srivastava & A. Izidoro 2025), raising the question of whether the NC chondrites, like their carbonaceous counterparts, also formed in a substructure of the disk. The NC chondrites, such as ordinary and enstatite chondrites, formed at around 2 Myr after solar system formation (e.g., N. Sugiura & W. Fujiya 2014), and their isotopic compositions indicate they formed in a different region of the disk than the carbonaceous chondrites, most likely in the inner disk (T. Kleine et al. 2020). Importantly, the NC chondrites are depleted in refractory inclusions compared to most carbonaceous chondrites (E. R. D. Scott & A. N. Krot 2014), but are rich in chondrules. Moreover, their chondrules exhibit distinct isotopic signatures from those of carbonaceous chondrites (J. M. Schneider et al. 2020). Our results are consistent with these observations, because at ∼2 Myr most of the mass in refractory inclusions and (CC-like) chondrules was concentrated in submillimeter-sized particles, which leads to their efficient trapping and hence limited transport to the inner disk (see also, e.g., S. J. Desch et al. 2018; P. Weber et al. 2018; T. Haugbølle et al. 2019; S. Jongejan et al. 2023; E. Van Clepper et al. 2025). Also, given that substructures in the disk act as traps mostly for rigid material, while more fragile material is transported away, the formation of NC chondrites in such substructures would naturally explain their high (NC-like) chondrule abundance. We thus speculate that the NC and carbonaceous chondrites formed in substructures inside and outside of the same planetary gap.

5. Conclusions

We have presented a model that integrates gas disk evolution, dust growth, and planetesimal formation while accounting for the different properties of dust components in carbonaceous chondrites. Our simulations show that differences in dust filtering and delivery rates to a planet-induced pressure bump can reproduce the matrix abundances relative to refractory inclusions and chondrules observed in carbonaceous chondrites over time (J. L. Hellmann et al. 2023). These results support a scenario in which carbonaceous chondrite parent bodies formed in a single, long-lived pressure bump, most likely located outside Jupiter's orbit.

In our model, chondrules and refractory inclusions stick to the matrix to form pebble-sized aggregates that can trigger planetesimal formation. Because refractory inclusions and chondrules are larger and more resistant to fragmentation than matrix grains, pressure bumps become enriched in these rigid components relative to matrix. In addition, larger particles drift inward faster, so material arriving from the outer disk becomes progressively more matrix-rich with time. This naturally explains the sequence from matrix-poor planetesimals (CO) to progressively more matrix-rich bodies (CV, CM, TL) in a pressure bump.

At later stages of disk evolution, when the gas density is low, collision velocities become too high for dust growth. In our simulations, matrix-poor planetesimals (analogous to CR chondrites) form from rigid monomers of tens of micrometers, whereas matrix-rich planetesimals form later from micrometer-sized matrix dust. Since during the disk dispersal the planetary gap opens, the formation of these matrix-rich planetesimals could extend to the outer disk.

Acknowledgments

The authors thank Jan Hellmann, Yves Marrocchi, Alessandro Morbidelli, and Fridolin Spitzer for valuable discussions. The authors also thank the anonymous referee for the comments that helped to improve the manuscript. J.D. and V.V. are funded by the European Union under the European Union's Horizon Europe Research & Innovation Programme 101040037 (PLANETOIDS). T.K. acknowledges the support from the ERC (project No. 101019380- HolyEarth).

Software: Astropy (Astropy Collaboration et al. 2013, 2018; Astropy Collaboration et al. 2022), numpy (C. R. Harris et al. 2020), matplotlib (J. D. Hunter 2007), DD-Diskevol (J. Drążkowska & C. P. Dullemond 2018) mcdust (V. Vaikundaraman et al. 2025).

Data and Code Availability

A curated subset containing all data necessary to interpret, verify, and extend the findings of this study has been deposited in Zenodo.[2] The code to reproduce the results and figures of this study is available at GitHub.[3]

Author Contributions

N.G. developed the model, performed the simulations, and led the writing of the manuscript. J.D. and T.K. conceived the project. J.D. and V.V. contributed an earlier version of the code. T.K. provided expertise on the isotopic composition of meteorites. All authors contributed to interpreting the results and reviewing the manuscript.

Appendix A
Supplementary Tables

In this appendix, we list the parameters employed in the gas (Table A1) and dust (Table A2) simulations presented in the main text.

Table A1
List of Parameters Employed in the Simulation of Gas Evolution

Symbol	Definition	Fiducial Values
$M_{\rm cloud}$	Molecular cloud mass	$1.15\,M_{\odot}$
$\Omega_{\rm cloud}$	Molecular cloud rotation rate	$10^{-14}\,{\rm s}^{-1}$
T_0	Background temperature	10 K
$\alpha_{\rm acc}$	Accretion viscosity coefficient	0.005
$r_{\rm planet}$	Planet location	5 au
$M_{\rm planet}$	Planet mass	$1\,M_{\rm Jup}$
$\alpha_{\rm acc}/\alpha_{\rm peak}$	Gap depth	1/1000
$t_{\rm planet,0}$	Planet formation init time	0.6 Myr
$t_{\rm planet,f}$	Planet formation final time	1.6 Myr
$t_{\rm photo}$	Photoevaporation activation time	1 Myr
⋯	Radial zones	2000
⋯	Standard grid range	$40\,R_{\odot}$ − 10 pc
⋯	High-resolution grid range	4–7 au
⋯	High-resolution steps	0.005 au

Note. Disk parameters not listed in this table are set to the fiducial values of the publicly available version of the code `DD-Diskevol`.

Table A2
List of Parameters Employed in the Simulation of Dust Evolution

Symbol	Definition	Fiducial Values
t_0	Initial time	2.19 Myr or 2 Myr after CAI
Z_0	Vertically integrated initial metallicity	$5\cdot10^{-5}$
$v_{\rm frag}$	Fragmentation velocity	$2\,{\rm m\,s}^{-1}$
$\alpha_{\rm t}$	Turbulent parameter	10^{-4}
$\rho_{\rm fragile}$	Internal density of fragile material	$1.2\,{\rm g\,cm}^{-3}$
$\rho_{\rm rigid}$	Internal density of rigid particles	$3.3\,{\rm g\,cm}^{-3}$
a_0	Radii of fragile monomers	10^{-4} cm
$a_{\rm rigid}^{\rm min} - a_{\rm rigid}^{\rm max}$	Radii range of rigid monomers	10^{-3}–10^{-1} cm
ζ	Rigid size power-law index	−3.9
$\bar{f}_{\rm ri}$	Initial mean rigid mass fraction	0.5
κ	Fragmentation power-law index	1/6
$\zeta_{\rm eff}$	Planetesimal formation efficiency	10^{-3}

Appendix B
Supplementary Figures

In this appendix, we provide the supplementary figures that complement the methods (Figure B1) results (Figures B2, B3 and B4) presented in the main text.

[2] zenodo.org/records/17176296
[3] github.com/nereagurru/CCformation

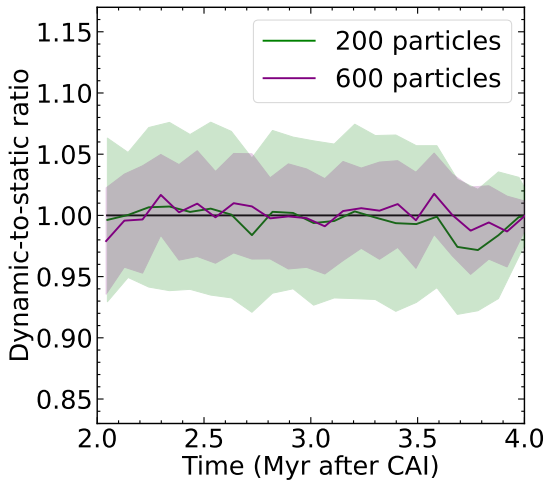

Figure B1. Evolution of the total dynamic rigid mass fraction in the zero-dimensional simulation compared to the static value, shown at different resolutions. The solid line indicates the mean ratio calculated over 0.1 Myr intervals, and the shaded regions show the corresponding standard deviation. In all cases, the dynamic value fluctuates around the static value, with oscillation amplitude decreasing as resolution increases.

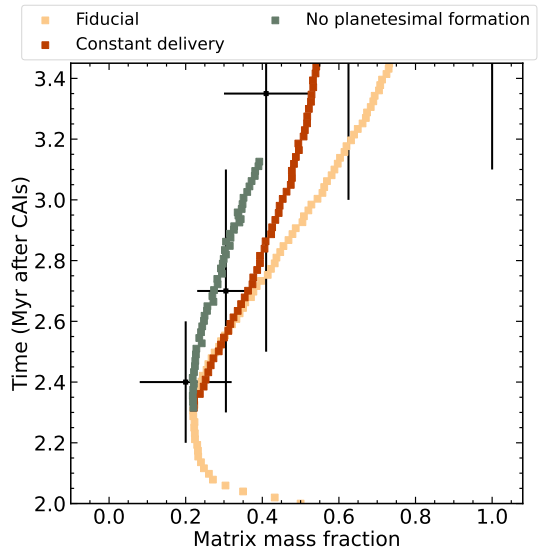

Figure B2. Matrix mass fraction of pebbles for three scenarios: (1) fiducial simulation from the main text; (2) constant rigid fraction of approximately 0.3 in the feeding flux from 2.3 Myr onward; and (3) same as (1) but without planetesimal formation. Simulation (3) is presented up to 3.1 Myr due to the increased computational cost at high dust-to-gas ratios. In (2), the matrix fraction increases less than in the fiducial case, as the replenishing material is richer in rigid particles. In (3), without planetesimal formation, the matrix mass fraction increases more slowly, mainly because the greater dust mass in the trap requires more time to alter its composition at a given feeding rate. These results highlight the importance of including decreasing rigid particle delivery and planetesimal formation in the model.

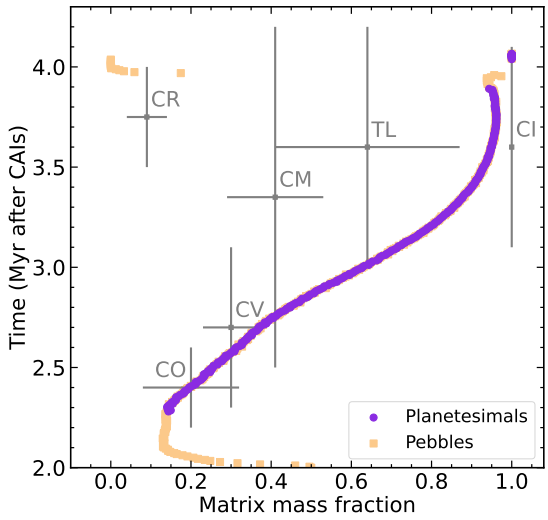

Figure B3. Matrix mass fraction of planetesimals for a top-heavy distribution of rigid particle sizes. The initial power-law index is assumed to be −2.9, in contrast to the index of −3.9 used in Figure 6. Initially, planetesimals have a lower matrix content due to the faster delivery and more efficient trapping of larger rigid particles. However, the matrix fraction increases more steeply over time as the supply of rigid particles to the dust trap becomes depleted. By approximately 3.9–4 Myr, the mean matrix mass fraction of pebbles in the trap decreases by the same process as in Figures 5 and 6, but the remaining rigid material is insufficient to trigger planetesimal formation.

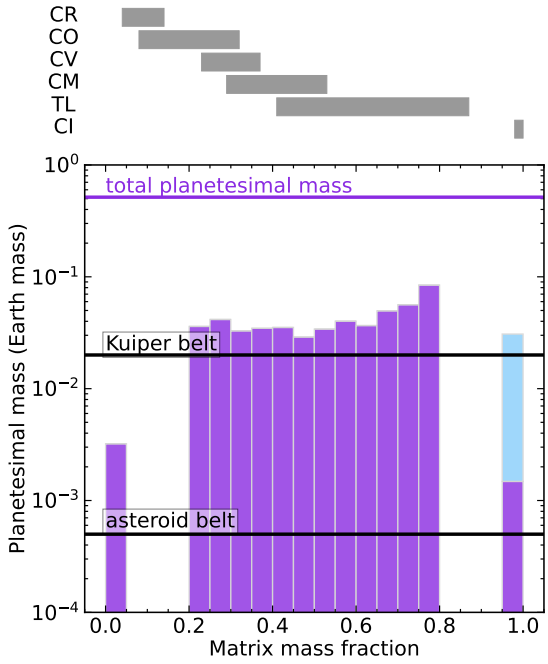

Figure B4. Mass of planetesimals formed at the pressure bump as a function of the matrix mass fraction in the fiducial simulation (purple bars). The potential planetesimal mass in the outer disk is also estimated by assuming all the remnant material in these regions could form planetesimals (light blue bar). Most planetesimals form with compositions similar to CO, CV, CM, or TL chondrites. CR-like and CI-like planetesimals at the local simulation account for roughly 0.6% and 0.2% of the total planetesimal mass. If we account for planetesimals forming in the outer regions as the gap widens, the CI abundance is expected to increase to at most 5%. The CR abundance may also increase if late-generation chondrules (i.e., conversion of fragile material to rigid one) are included. The simulated total planetesimal mass and the estimated masses of the asteroid belt (F. E. DeMeo & B. Carry 2013) and the Kuiper Belt (E. V. Pitjeva & N. P. Pitjev 2018) are shown for comparison.

ORCID iDs

Nerea Gurrutxaga https://orcid.org/0009-0008-3256-9564
Joanna Drążkowska https://orcid.org/0000-0002-9128-0305
Vignesh Vaikundaraman https://orcid.org/0000-0002-2451-9574
Thorsten Kleine https://orcid.org/0000-0003-4657-5961

References

Alexander, C. M. O. 2019, GeCoA, 254, 277
Andrews, S. M., Huang, J., Pérez, L. M., et al. 2018, ApJL, 869, L41
Ansdell, M., Williams, J. P., van der Marel, N., et al. 2016, ApJ, 828, 46
Arakawa, S., & Nakamoto, T. 2019, ApJ, 877, 84
Astropy Collaboration, Price-Whelan, A. M., Lim, P. L., et al. 2022, ApJ, 935, 167
Astropy Collaboration, Price-Whelan, A. M., Sipőcz, B. M., et al. 2018, AJ, 156, 123
Astropy Collaboration, Robitaille, T. P., Tollerud, E. J., et al. 2013, A&A, 558, A33
Bai, X.-N., & Stone, J. M. 2010, ApJ, 722, 1437
Barnes, J. J., Nguyen, A. N., Abernethy, F. A. J., et al. 2025, NatAs, 9, 1785
Beitz, E., Güttler, C., Weidling, R., & Blum, J. 2012, Icar, 218, 701
Bell, K. R., & Lin, D. N. C. 1994, ApJ, 427, 987
Birnstiel, T. 2024, ARA&A, 62, 157
Birnstiel, T., Klahr, H., & Ercolano, B. 2012, A&A, 539, A148
Brasser, R., & Mojzsis, S. J. 2020, NatAs, 4, 492
Bryson, J. F. J., & Brennecka, G. A. 2021, ApJ, 912, 163
Budde, G., Kruijer, T. S., & Kleine, T. 2018, GeCoA, 222, 284
Carrera, D., Gorti, U., Johansen, A., & Davies, M. B. 2017, ApJ, 839, 16
Ciesla, F. J. 2006, MAPS, 41, 1347
Ciesla, F. J. 2007, Sci, 318, 613
Colas, F., Zanda, B., Bouley, S., et al. 2020, A&A, 644, A53
Cuzzi, J. N., Davis, S. S., & Dobrovolskis, A. R. 2003, Icar, 166, 385
DeMeo, F. E., & Carry, B. 2013, Icar, 226, 723
Desch, S. J., Kalyaan, A., & O'D. Alexander, C. M. 2018, ApJS, 238, 11
Dohnanyi, J. S. 1969, JGR, 74, 2531
Drążkowska, J., Alibert, Y., & Moore, B. 2016, A&A, 594, A105
Drążkowska, J., Bitsch, B., Lambrechts, M., et al. 2023, ASPC, 534, 717
Drążkowska, J., & Dullemond, C. P. 2018, A&A, 614, A62
Drążkowska, J., Windmark, F., & Dullemond, C. P. 2013, A&A, 556, A37
Dunham, E. T., Sheikh, A., Opara, D., et al. 2023, MAPS, 58, 643
Ercolano, B., Jennings, J., Rosotti, G., & Birnstiel, T. 2017, MNRAS, 472, 4117
Eriksson, L. E. J., Johansen, A., & Liu, B. 2020, A&A, 635, A110
Fukuda, K., Tenner, T. J., Kimura, M., et al. 2022, GeCoA, 322, 194
Gillespie, D. T. 1975, JAtS, 32, 1977
Gunkelmann, N., Kataoka, A., Dullemond, C. P., & Urbassek, H. M. 2017, A&A, 599, L4
Güttler, C., Blum, J., Zsom, A., Ormel, C. W., & Dullemond, C. P. 2010, A&A, 513, A56
Harris, C. R., Millman, K. J., van der Walt, S. J., et al. 2020, Natur, 585, 357
Hartmann, L., Calvet, N., Gullbring, E., & D'Alessio, P. 1998, ApJ, 495, 385
Haugbølle, T., Weber, P., Wielandt, D. P., et al. 2019, AJ, 158, 55
Hellmann, J. L., Hopp, T., Burkhardt, C., & Kleine, T. 2020, E&PSL, 549, 116508
Hellmann, J. L., Schneider, J. M., Wölfer, E., et al. 2023, ApJL, 946, L34
Hopp, T., Dauphas, N., Abe, Y., et al. 2022, SciA, 8, eadd8141
Houge, A., & Krijt, S. 2023, MNRAS, 521, 5826
Houge, A., Johansen, A., Banzatti, A., & Grant, S. 2026, arXiv.2604.11925
Hueso, R., & Guillot, T. 2005, A&A, 442, 703
Hunter, J. D. 2007, CSE, 9, 90
Jacquet, E., & Thompson, C. 2014, ApJ, 797, 30
Johansen, A., Blum, J., Tanaka, H., et al. 2014, in Protostars and Planets VI, ed. H. Beuther et al. (Univ. of Arizona Press), 547
Jones, R. H. 2012, MAPS, 47, 1176
Jongejan, S., Dominik, C., & Dullemond, C. P. 2023, A&A, 679, A45
Kleine, T., Budde, G., Burkhardt, C., et al. 2020, SSRv, 216, 55
Kleine, T., Mezger, K., Palme, H., Scherer, E., & Münker, C. 2005, GeCoA, 69, 5805
Krijt, S., Ciesla, F. J., & Bergin, E. A. 2016, ApJ, 833, 285
Krot, A. N., Amelin, Y., Bland, P., et al. 2009, GeCoA, 73, 4963
Kruijer, T. S., Burkhardt, C., Budde, G., & Kleine, T. 2017, PNAS, 114, 6712
Kruijer, T. S., Touboul, M., Fischer-Gödde, M., et al. 2014, Sci, 344, 1150
Lau, T. C. H., Birnstiel, T., Drążkowska, J., & Stammler, S. M. 2024, A&A, 688, A22
Lauretta, D. S., Connolly, H. C., Aebersold, J. E., et al. 2024, MAPS, 59, 2453
Lega, E., Morbidelli, A., Masset, F., & Béthune, W. 2025, A&A, 702, A45
Lim, J., Simon, J. B., Li, R., et al. 2024, ApJ, 969, 130
Machii, N., Nakamura, A. M., Güttler, C., Beger, D., & Blum, J. 2013, Icar, 226, 111
Marrocchi, Y., Piralla, M., Regnault, M., et al. 2022, E&PSL, 593, 117683
Morbidelli, A., & Crida, A. 2007, Icar, 191, 158
Morbidelli, A., Marrocchi, Y., Ahmad, A. A., et al. 2024, A&A, 691, A147
Ormel, C. W., Cuzzi, J. N., & Tielens, A. G. G. M. 2008, ApJ, 679, 1588
Pfeil, T., Armitage, P. J., & Jiang, Y.-F. 2025, ApJ, 994, 272
Picogna, G., Ercolano, B., & Espaillat, C. C. 2021, MNRAS, 508, 3611
Pinilla, P., Benisty, M., & Birnstiel, T. 2012, A&A, 545, A81
Pinte, C., Teague, R., Flaherty, K., et al. 2023, ASPC, 534, 645
Pitjeva, E. V., & Pitjev, N. P. 2018, CeMDA, 130, 57
Schneider, J. M., Burkhardt, C., Marrocchi, Y., Brennecka, G. A., & Kleine, T. 2020, E&PSL, 551, 116585
Schrader, D. L., Nagashima, K., Krot, A. N., et al. 2017, GeCoA, 201, 275
Scott, E. R. D., & Krot, A. N. 2014, in Meteorites and Cosmochemical Processes, ed. A. M. Davis, 1 (Elsevier), 65
Shakura, N. I., & Sunyaev, R. A. 1973, A&A, 24, 337
Simon, J. B., Armitage, P. J., Li, R., & Youdin, A. N. 2016, ApJ, 822, 55
Simon, S. B., & Grossman, L. 2015, MAPS, 50, 1032
Spitzer, F., Hopp, T., Burkhardt, C., Dauphas, N., & Kleine, T. 2025, E&PSL, 667, 119530
Spitzer, F., Kleine, T., Burkhardt, C., et al. 2024, SciA, 10, eadp2426
Srivastava, B., & Izidoro, A. 2025, SciA, 11, eady4823
Stammler, S. M., Drążkowska, J., Birnstiel, T., et al. 2019, ApJL, 884, L5
Stammler, S. M., Lichtenberg, T., Drążkowska, J., & Birnstiel, T. 2023, A&A, 670, L5
Sugiura, N., & Fujiya, W. 2014, MAPS, 49, 772
Umstätter, P., Gunkelmann, N., Dullemond, C. P., & Urbassek, H. M. 2019, MNRAS, 483, 4938
Umstätter, P., & Urbassek, H. M. 2021, A&A, 652, A40
Vaikundaraman, V., Gurrutxaga, N., & Drążkowska, J. 2025, arXiv: 2507.21239
Van Clepper, E., Price, E. M., & Ciesla, F. J. 2025, ApJ, 980, 201
Weber, P., Benítez-Llambay, P., Gressel, O., Krapp, L., & Pessah, M. E. 2018, ApJ, 854, 153
Weiss, B. P., Bai, X.-N., & Fu, R. R. 2021, SciA, 7, eaba5967
Yokoyama, T., Nagashima, K., Nakai, I., et al. 2023, Sci, 379, abn7850
Youdin, A. N., & Goodman, J. 2005, ApJ, 620, 459
Zsom, A., & Dullemond, C. P. 2008, A&A, 489, 931